J Mater Sci (2006) 41:4512–4522
DOI 10.1007/s10853-006-0084-x

Quantitative characterization of nanoprecipitates in irradiated low-alloy steels: advances in the application of FEG-STEM quantitative microanalysis to real materials

M. G. Burke · M. Watanabe · D. B. Williams · J. M. Hyde

Received: 31 December 2005 / Accepted: 1 March 2006 / Published online: 29 June 2006

Abstract The characterization of the solute-enriched features (clusters or nanoprecipitates in irradiated low-alloy steels) requires extremely high spatial and elemental resolution, previously necessitating analysis using atom probe field-ion microscopy. In this investigation, field-emission gun-scanning transmission electron microscope (FEG-STEM) quantitative energy dispersive X-ray (EDX) microanalysis (spectrum imaging) has been applied to the characterization of the irradiation-induced nanoprecipitates in a low-alloy forging steel. Refinements in the EDX data have been possible via the application of multivariate statistical analysis (MSA) to the spectrum images, resulting in significantly reduced noise in the images. Most importantly, MSA permitted the clear identification of other elements in these Ni-enriched nanoprecipitates—including Mn and Cu. The processed X-ray spectrum images also provided direct evidence of the preferential formation of these irradiation-induced features along pre-existing dislocations within the steel, as well as the formation of intragranular nanoprecipitates. This research has provided the first direct X-ray spectrum images of irradiation-induced nanoprecipitates in high Ni A508 Gr4N forging steel, and has demonstrated the significant improvements attainable though the application of MSA techniques to the spectrum images. These results independently confirmed the analyses of the Ni-enriched nanoprecipitates previously conducted by 3D-APFIM, with the performance of the FEG-STEM/EDX technique shown to be comparable to that of the 3D-APFIM technique.

M. G. Burke
Bechtel Bettis, Inc., P.O. Box 79, West Mifflin, PA 15122, USA

M. Watanabe (✉) · D. B. Williams
Department of Materials Science and Engineering/Center for Advanced Materials and Nanotechnology, Lehigh University, Bethlehem, PA 18015, USA
e-mail: masashi.watanabe@lehigh.edu

J. M. Hyde
Department of Materials, University of Oxford, Parks Road, Oxford OX1 3PH, UK

Introduction

Neutron irradiation can cause significant changes in the microstructure and mechanical properties of low-alloy steels. Irradiation damage in low-alloy steels and welds has been studied for approximately 40 years. Irradiation produces a hardening of the steel, the extent of which is sensitive to alloy composition, particularly to the Cu, Mn and Ni content of the steel. This irradiation-induced hardening reflects an increase in yield strength of the steel, and can lead to a reduction in toughness of the steel. Typically, the extent of irradiation damage is assessed using Charpy V-Notch specimens tested at a series of temperatures to determine the impact energy as a function of temperature. Irradiation leads to an increase in the ductile-to-brittle transition temperature, and a decrease in the upper shelf energy. Most of the materials research in the area of irradiation effects has concentrated on the manifestation of damage via mechanical property measurements, and the characterization of damage. In particular, the formation of defects such as dislocation loops, voids, nanocavities, etc. has been studied using techniques such as transmission electron microscopy (TEM), small-angle neutron scattering, and positron-annihilation spectroscopy. Although it has been possible to measure the change in mechanical

properties caused by irradiation, it has not been possible to specifically identify, using TEM, the feature(s) within the microstructure that were responsible for the mechanical behavior.

It has now been established that irradiation induces the formation of solute-enriched features that contribute to the hardening in low-alloy steels, and leads to a degradation in mechanical properties. The first direct detection of the irradiation-induced hardening features occurred in the 1980s using atom probe field-ion microscopy (APFIM) [1, 2]. The observed irradiation-induced features were ultrafine, solute-enriched ''clusters'', which contained high levels of iron. Since that time, APFIM has been the only technique for measuring these features, with major advances due to the development of 3D atom probes [3–6]. The high spatial resolution of the atom probe coupled with its elemental sensitivity has permitted the microchemical analysis of these features. It should be noted, however, that the volume analyzed in a typical specimen is limited. New developments in atom probe design, such as the local electrode atom probe, are addressing this limitation [7, 8]. However, direct observation of the microstructure, including measurement of the local composition, within a single instrument, e.g. a S/TEM, would be preferable.

The objective of this study was to determine whether it is experimentally possible to independently identify irradiation-induced solute-enriched nanoprecipitates in an irradiated A508 Gr4N steel using a dedicated field-emission gun-scanning transmission electron microscope (FEG-STEM). This paper reports the results of direct characterization of an irradiated low-alloy A508 Gr4N steel that had been previously comprehensively characterized by a combination of TEM and APFIM techniques. The observations were made using the Lehigh University VG HB603 FEG-STEM equipped with an Oxford Instruments EDX system. Subsequent analysis of the EDX data was performed using multivariate statistical analysis (MSA) coupled with the ζ(zeta)-factor method for EDX quantification. The results of the FEG-STEM/EDX analyses were compared to those previously obtained using the combined 3D-APFIM technique to validate this new method of detailed material characterization.

Material and prior characterization

The steel studied in this investigation was a low-alloy A508 Gr4N forging steel, the composition of which is listed in Table 1. The A508 Gr4N steel had been quenched from 927 °C followed by tempering at ~615 °C. The steel was subsequently irradiated under low flux conditions to a damage level of 68 millidisplacements per atom (mdpa) at approximately 250 °C.

Table 1 Nominal compositions of the low-alloy steel A508 Gr4N (wt%)

C	Mn	Ni	Si	Cr	Mo	Cu	Al	P	S	N	Fe
0.18	0.29	3.75	0.03	1.59	0.57	0.08	0.003	0.009	0.011	~50 ppm	bal.

Prior to this study, the material had been characterized using a variety of techniques, including TEM, 3D-APFIM, and positron annihilation lineshape analysis [2]. The general microstructure was a mixed tempered martensite-tempered bainite structure. Representative micrographs are presented in Fig. 1 showing this mixed tempered microstructure. Copious carbide precipitation (predominantly Fe-rich M_3C and Cr-enriched M_7C_3, with some Cr-enriched $M_{23}C_6$) was observed throughout the structure. A limited amount of fine Mo-enriched M_2C was non-uniformly distributed within the overall microstructure. Fig. 2 contains STEM images of the steel irradiated to 68 mdpa. The fine lath structure coupled with numerous dislocations and carbides (both interlath and intralath) provides numerous sinks for irradiation-induced vacancies so that ''black spot'' damage or dislocation loops are not observed for the irradiation condition studied. TEM characterization provided no clear evidence of irradiation-induced microstructural changes.

To identify the physical changes in the steel due to irradiation, an extensive investigation had been performed to characterize the nature of irradiation damage in this steel [2]. 3D atom probe analysis of the steel was performed using the Oxford University optical position sensitive atom probe to identify the presence of irradiation-induced solute-related hardening features in the microstructure. The 3D atom probe field-ion microscope used in that investigation contained a position-sensitive detector, consisting of a silicon diode array (256×256) and an anode array (10×8). The field-evaporated ions from the specimen hit a phosphor screen, and the resulting photons were split using a partially reflecting mirror. One part was detected by the diode array, which was used to calculate the positions of impact on the detector accurately. The remaining photons were detected by the anode array to yield accurate flight times (for the time-of-flight mass spectrometer). A map between the two detectors was then used to correlate impact positions and flight times. This detector is capable of detecting up to 8 ions per pulse. This instrument also has improved mass resolution (to approximately 1 in 600) over the original position-sensitive atom probe [4].

After acquisition, the acquired data were analyzed and corrected for noise in the mass spectrum. A correction was also made for unpositioned detection events, and for noise-related events. The resulting corrected dataset from the analyzed volume was reconstructed for each element detected. This is analogous to a spectrum image. Within the

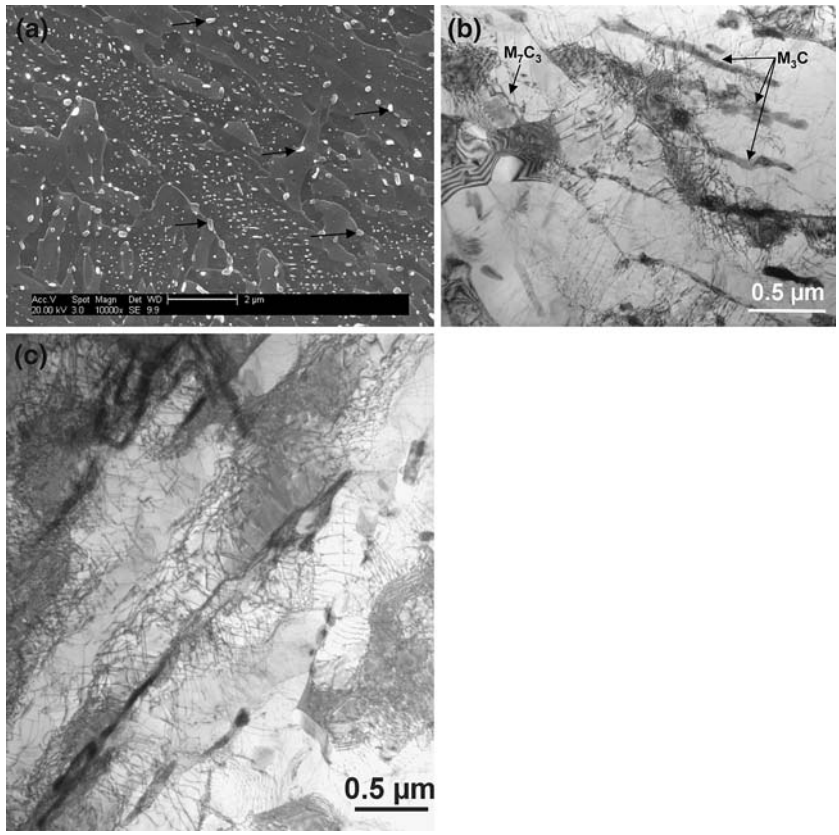

Fig. 1 (**a**) Secondary and (**b**), (**c**) transmission electron images obtained from unirradiated A508 Gr4N steel. Note the mixed tempered martensite-tempered bainite microstructure. Several $M_{23}C_6$ carbides are arrowed in (**a**); M_3C and M_7C_3 carbides are labeled in (**b**)

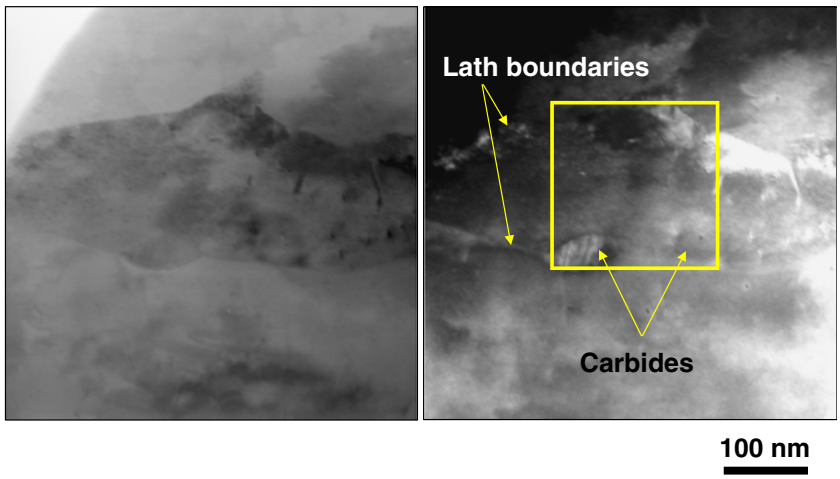

Fig. 2 (**a**) BF- and (**b**) ADF-STEM images of the neutron-irradiated low-alloy steel. No irradiation-induced defects were readily observable in this complex, tempered lath structure

analyzed volume, enrichments or depletions could then be detected. The local composition was then determined simply by summing up the number of ions of a given element and dividing by the total number of ions detected within that volume. Thus, the composition of a volume of 1 nm^3 could be determined directly. In that study, a recursive search algorithm was used to identify the nano-precipitates within specific analyzed volumes. Subsequent reanalysis of the atom probe data set was performed to evaluate the distribution of solute within the analyzed volume, and to identify the presence of solute-enriched features.

In the A508 Gr4N irradiated steel, distinct solute-enriched features were detected. These features appeared to be more well defined than the irradiation-induced solute-enriched ''clusters'' which had been previously observed in low-alloy steels and welds irradiated under other conditions [9–11]. They were thus termed ''nanoprecipitates''. The nanoprecipitates observed in this A508 Gr4N steel varied in size from ~1 to 4 nm, with an average size of

~2 nm. The mean composition was approximately 28% Ni–10% Mn–4% Cu–3% Si–55% Fe. The analysis of a 1 nm^3 volume in the center of a 4 nm diameter nanoprecipitate yielded a composition with an increased Ni and Mn content: 32% Ni–15% Mn–6% Cu–5% Si–42% Fe, indicating compositional variation within the feature. Figure 3 shows a reconstruction of an analyzed nanoprecipitate. Based on the volume of specimen analyzed in the atom probe, the approximate number density of irradiation-induced nanoprecipitates was $\sim 5 \times 10^{23}$ m^{-3}. Further samples of this material have now been characterized using FEG-STEM X-ray spectrum imaging in this study.

Experimental

Specimens for analytical electron microscopy (FEG-STEM EDX) were prepared using a conventional jet polishing technique. General microstructural characterization was performed using a Philips CM300 field-emission gun (FEG) analytical electron microscope (AEM) operated at 300 kV, and an FEI Tecnai F20 FEG AEM operated at 200 kV. High spatial resolution quantitative energy dispersive X-ray microanalysis was performed using the Lehigh University Vacuum Generators HB603 dedicated FEG-STEM operated at 300 kV, and equipped with an Oxford Instruments EDX spectrometer and INCA analysis system. This special HB603 FEG-STEM is optimized for EDX microanalysis, with a solid angle of 0.3 steradian.

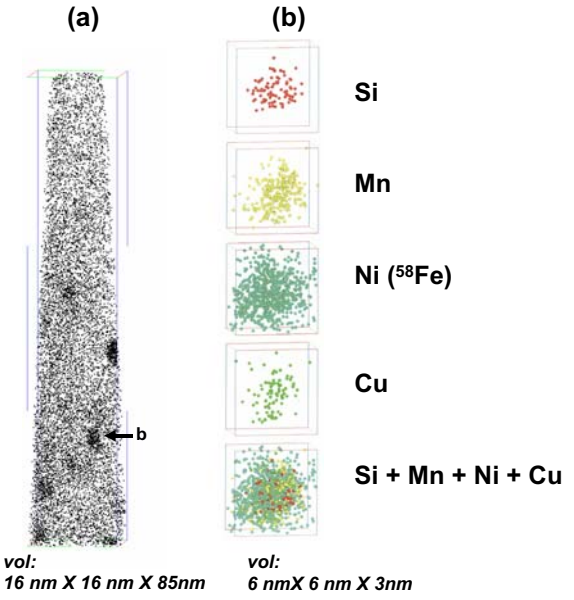

Fig. 3 (**a**) 3D-atom probe reconstruction of the analysis volume showing the field-evaporated Ni(+^{58}Fe) ions from the irradiated A508 Gr4N steel [2]. Note the presence of Ni-enriched nanoprecipitates. (**b**) 3D-atom probe reconstruction of an irradiation induced nanoprecipitate showing the various elements detected in the feature (Fe not shown)

Characterization via X-ray analysis in FEG-STEM

Acquisition of X-ray spectrum images

All microanalytical characterization of the electron-transparent low-alloy steel specimens was performed using the HB603 FEG-STEM. In order to analyze the fine-scale nanoprecipitates induced by irradiation, X-ray spectrum imaging was used instead of the conventional energy-window method at 300 keV with the probe current of 0.5–0.7 nA in the probe of 1.5 nm (full width at tenth maximum (FWTM)). All spectrum images (SIs) were acquired with 128×128 pixels and 1024 channels (20 eV/channel dispersion) for a dwell time of 400 ms per pixel (total acquisition: ~90 min). One of the major advantages in spectrum imaging is the capability of post-acquisition processing of the elemental maps with regular spectral-processing techniques [12, 13]. In this way, minor signals from unexpected elements, which were not considered for mapping beforehand, can be imaged after the acquisition. Thus, SI is becoming an increasingly important tool for materials characterization, in combination with advanced statistical analysis described in the following sections.

Application of principal component analysis (PCA) to X-ray SIs

Before quantification, principal component analysis (PCA) was applied to the X-ray SIs. PCA is one of the multivariate statistical analysis (MSA) techniques that can be used to identify any statistically significant features in large data sets (such as spectrum images) and to reduce random-noise components efficiently in a statistical manner [e.g. 14, 15]. This family of techniques has been used in a wide range of studies to gain insight into spectral data in electron microscopy [e.g. 16–19]. The general concept of PCA is to reduce the dimensionality of an original large dataset by finding a minimum number of variables, which can still describe the original dataset without loosing significant information [14]. This approach is well suited for the SI dataset since some variables are not always known prior to analysis. In addition, the typical size of SI datasets is too large to seek individual pixels or individual energy channels. Therefore, any technique that can assist in the identification of such variables from a large dataset is essential. In this study, PCA was applied (1) to identify specific features in the X-ray SI, and (2) to reduce the random noise components in the SI in a statistical manner.

Quantification of X-ray spectrum images

The elements Fe, Cr, Ni, Mn, Cu and Mo in this low-alloy steel were quantified from the spectrum images. The X-ray intensities of the characteristic Kα lines of the elements of interest were extracted as images from the measured X-ray SIs using an energy-window method, i.e. the X-ray intensities at specific characteristic peaks were obtained from the SIs by selecting the corresponding energy ranges. Background intensities were also measured at lower and higher energy regions around each characteristic X-ray peaks, and then the average of the two background intensities was subtracted from the corresponding peak intensity. It should be noted that there are significant peak overlaps between the Mn Kα and Cr Kβ lines and between the Ni Kβ and Cu Kα lines in this system. An ordinary energy window cannot separate these overlaps. Therefore, in this study, both the intensities of Mn Kα and Cr Kβ lines and of Ni Kβ and Cu Kα lines were extracted together from single wide-energy windows, respectively. Next, the β line intensities of Cr and Ni determined from the peak intensities of the corresponding α lines by multiplying the relative intensity ratios (for Cr, $\alpha{:}\beta = 0.8832{:}\ 0.1168$; for Ni, $\alpha{:}\beta = 0.8790{:}\ 0.1210$) [20] were subtracted from the overlapped intensities, respectively. For quantification of those extracted intensity maps, the ζ-factor method [21–23] was applied, which can provide not only compositions but also specimen thickness simultaneously. The ζ-factors required for quantification of this alloy were determined from the National Institute of Standards and Technology (NIST) thin-film glass standard reference material (SRM) 2063a [24]. The details of the ζ-factor method and the ζ-factor determination can be found in [21–23].

Results and discussion

Improvement of X-ray map quality by PCA

An X-ray SI was acquired from an area surrounded with a dashed box in Fig. 2b. Fig. 4 shows a set of composition maps quantified from the original X-ray SI (a: Fe, b: Cr, c: Ni, d: Mn, e: Cu and f: Mo). There are two Cr-enriched regions at the bottom of the field of view. These Cr enrichments correspond to alloy carbides, and composition-depleted areas in the Fe and Ni maps are superimposed accordingly. The elemental enrichments are also evident in the Mn and Mo maps as well. In addition to the carbides, the localized Ni enrichments and corresponding Fe depletions can be seen in Fig. 4; these Ni-enrichments are consistent with the irradiation-induced ultrafine nanoprecipitates. As mentioned previously, these precipitates are not visible in either the TEM or in the STEM images. However, any microchemical information in the maps for Mn, Cu and Mo is obscured by the noise, despite the fact that Cu and Mn enrichment of the nanoprecipitates was confirmed independently by 3D-APFIM. The distribution of the minor elements below 3 wt% in this case can never be imaged properly with such short acquisition times in the STEM-based elemental-mapping approach.

The poor analytical sensitivity in elemental mapping can be offset by spectrum imaging combined with the PCA techniques. By applying PCA, the SI dataset $\mathbf{D}_{((x,\ y),\ E)}$ with the spatial information (x, y) and the energy-channel (i.e. spectral) information (E) can be decomposed as [14, 15]:

$$\mathbf{D}_{((x,y),E)} = \mathbf{S}_{((x,y),n)} \times \mathbf{L}^{\mathrm{T}}_{(E,n)} \tag{1}$$

where $\mathbf{L}_{(E,\ n)}$ and $\mathbf{S}_{((x,\ y),\ n)}$ are called loading and score matrices, respectively. Specifically, in the SI dataset each row of $\mathbf{L}$ contains a spectral feature uncorrelated to other row information (spectral features). The superscript T of the matrix $\mathbf{L}$ represents a matrix transpose. On the other hand, each row of $\mathbf{S}$ represents a spatial amplitude of the corresponding loading spectrum. The individual product of each row of the loading and score matrices is called a component. n is the number of the components and can mathematically be equal or less than the smaller number of $(x \times y)$ or E. Before decomposing the SI data, spatial and spectral scaling based on the Poisson counting statistics [24, 25] was applied to enhance minor fluctuations of the characteristic X-ray peaks in individual spectra. The general concept of PCA is to reduce the dimensionality of an original large dataset by finding a minimum number of components which can still describe the original dataset without losing major information [14]. The major features are called the ''principal components''. The data decomposition described in Eq. (1) can also provide eigenvalues of the SI data matrix $\mathbf{D}_{((x,\ y),\ E)}$, whose relative magnitudes represent the fraction of information of the corresponding component contained in the dataset. Therefore, a number of the principal components can be determined by evaluating the magnitude of eigenvalues. One of the most common approaches is a use of a graphical plot of logarithms of the eigenvalues against the component, the ''scree plot''.

The scree plot of the X-ray SI acquired from the square region in Fig. 2b is shown in Fig. 5. In this scree plot, at least the first 6 components can be easily distinguished from the noise components that are expressed as a straight line in the higher-index component side. The #7 component must be evaluated as to whether it is a principal component or not. Fig. 6 shows selected pairs of the loading spectra and the corresponding score images of the components in this SI (a: #1, b: #2, c: #5 and d: #7). The most significant component in the dataset is always the average, and hence the loading spectrum of #1 component (Fig. 6a) represents

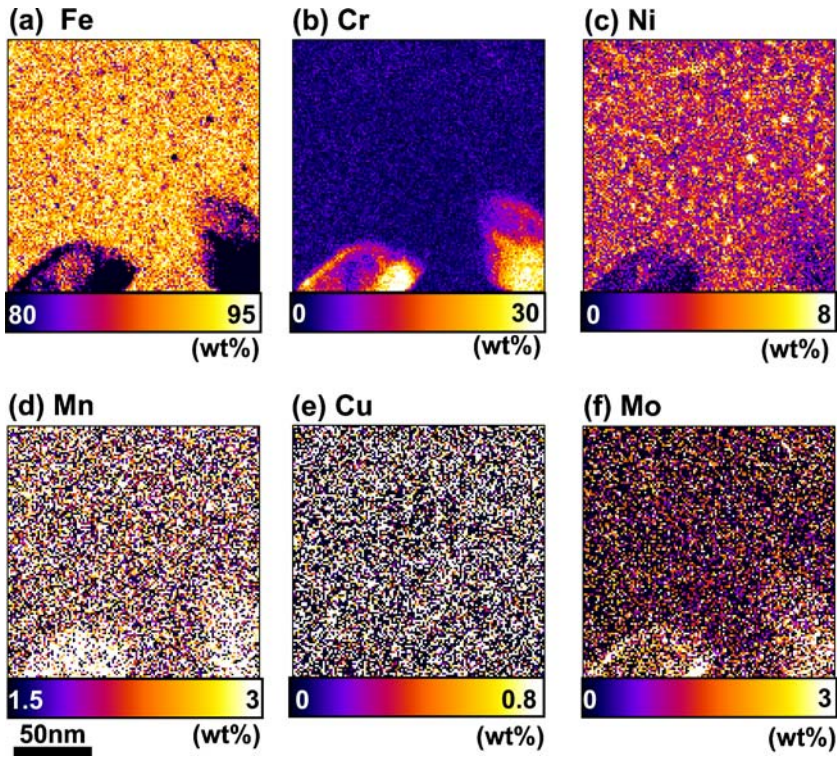

Fig. 4 Compositional maps of the neutron-irradiated low-alloy steel quantified from the original X-ray SI, acquired from the area selected in Fig. 2c: (**a**) Fe, (**b**) Cr, (**c**) Ni, (**d**) Mn, (**e**) Cu and (**f**) Mo

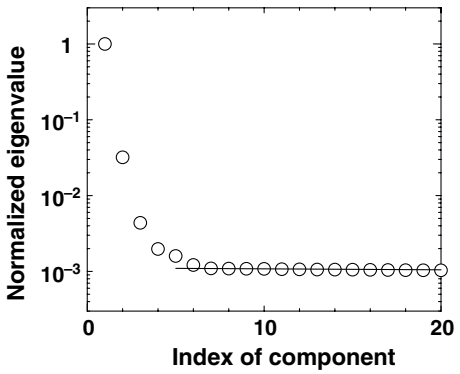

Fig. 5 Normalized eigenvalues of the X-ray SI taken at the squared box in Fig. 2b, plotted against the component determined by PCA (scree plot)

the average spectrum of the X-ray SI. Any component higher than #1 indicates any significant difference from the average. Therefore, the loading spectra after the #1 component contain positive and negative peaks, which are not physically meaningful but interpretable expressions. The #2 loading spectrum has positive Cr Kα and negative Fe Kα and Ni Kα peaks. The bright regions in the corresponding score image enhance this spectral feature and hence this component represents the carbides. The #5 loading spectrum shows positive Ni L, Mn K, Ni K and Cu K peaks and a negative Fe K peak, and the bright regions in the score image are superimposed on the ultrafine precipitate positions in the Ni map (Fig. 4c). Thus, the #5 component represents the irradiation-induced ultrafine nanoprecipitates. According to the #5 loading spectrum, the ultrafine nanoprecipitates contain Ni, Mn and Cu, which agrees with the results obtained by the 3D-APFIM analysis. The #7 component does not show specific features as expected from the scree plot.

Once the principal and noise components are distinguished, the original SI data can be expressed with the limited number of the principal components α, instead of the number of the total components n:

$$\tilde{\mathbf{D}}_{((x,y),E)} = \mathbf{S}_{((x,y),\alpha)} \times \mathbf{L}^{\mathrm{T}}_{(E,\alpha)} \quad (2)$$

where $\tilde{\mathbf{D}}$ is the reconstructed data matrix with the limited number of the principal components α ($\ll n$, in this case $\alpha = 6$ out of 1024). As a result of the data reconstruction, the random-noise parts can be efficiently removed from the original SI without degrading the spatial or energy resolution. A series of composition maps quantified from the PCA-reconstructed SI are shown in Fig. 7 in the same format as Fig. 4. Comparison of Fig. 7 with the original maps in Fig. 4, clearly demonstrates the efficient removal of the noise. In the Fe map, the local depletions corresponding to the ultrafine nanoprecipitates are clearer. More importantly, the ultrafine nanoprecipitates are now clearly revealed in the Ni, Mn and Cu maps. In addition, the distribution of Cr and Mo in the carbides is also clearer. These elemental distributions, especially for the minor constituents such as Mn, Cu and Mo were not clearly visible in the original maps in Fig. 4, due to the high noise

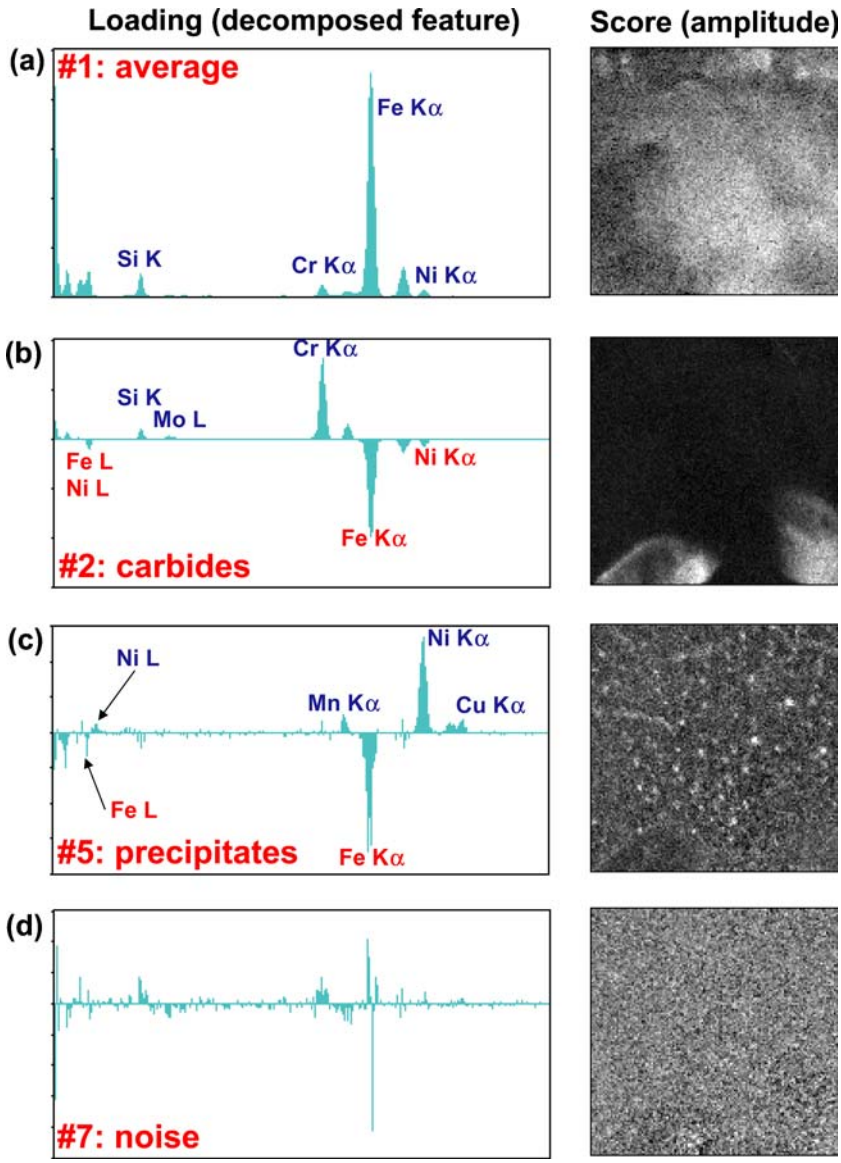

Fig. 6 Selected pairs of the loading spectra and the corresponding score images of the components in the SI (of area shown in Fig. 2b) (**a**: #1, **b**: #2, **c**: #5 and **d**: #7)

components in the unprocessed SI. However, these elemental maps, taken with relatively short acquisition times, are significantly improved by the combination of SI and PCA reconstruction. Now, small compositional changes, even below 1 wt%, are detectable in the map without degrading the high spatial resolution. This clearly demonstrates that quantitative maps of the minor elements can now be obtained using these techniques.

The nanoprecipitates observed in the X-ray maps ranged from 2 to 4 nm in size. Based on the thickness of the area mapped, the number density of irradiation-induced nanoprecipitates was estimated to be $\sim 2 \times 10^{23}$ m^{-3}, which agrees well with the number density reported via 3D-APFIM of $\sim 5 \times 10^{23}$ m^{-3}. It is noted that nanoprecipitates ranging from ~1 to 4 nm were identified via 3D-APFIM, but the FEG-STEM EDX maps showed nanoprecipitates ranging from ~2 to 4 nm in size.

Advanced microchemical information extracted from quantified X-ray maps

As described previously, EDX spectra quantification using the ζ-factor method can also provide specimen-thickness data as a function of analysis location. By combining the specimen thickness information with the measured composition, additional microchemical data can be extracted. An example of this advanced analysis is shown in Fig. 8, which contains atom maps converted from the composition maps in Fig. 7 (a: specimen thickness map, b: spatial resolution map, c: map of the number of total atoms, d: map of the number of Ni atoms, e: map of the number of Mn atoms and f: map of the number of Cu atoms).

The calculation of the spatial resolution R requires information about the incident beam size and beam broadening (i.e. the compositions and thickness).

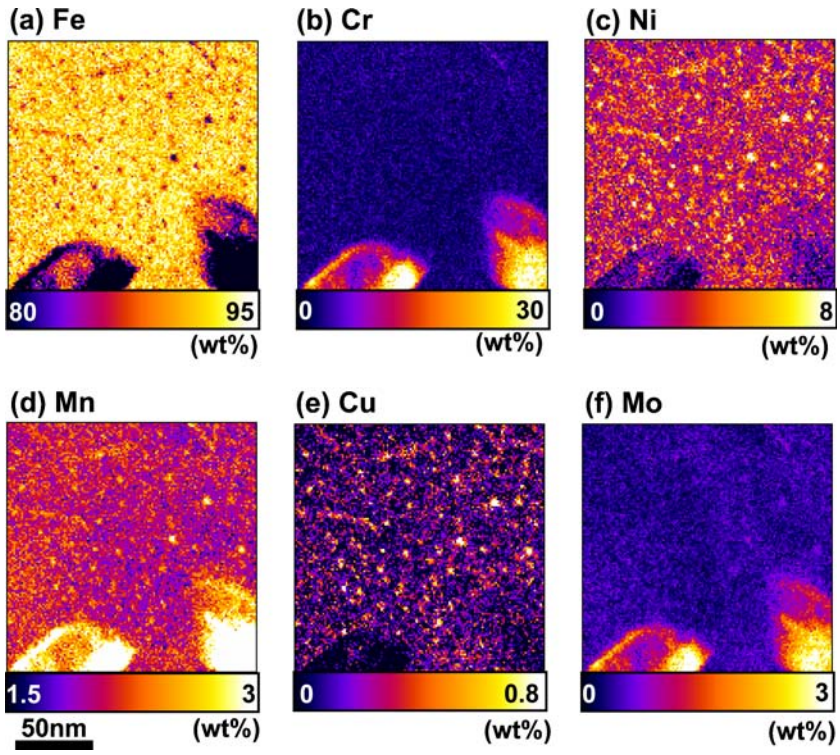

Fig. 7 Compositional maps of the neutron-irradiated low-alloy steel from the same X-ray SI improved by the PCA-reconstruction. Random noise components in the original maps were efficiently removed by applying the PCA reconstruction, in the same format as Fig. 4

According to Keast and Williams [27], the Gaussian beam-broadening model [28] is the best description of the beam-specimen interaction volume and the spatial resolution. The spatial resolution based on the Gaussian beam-broadening model can be given as [29]:

$$R = 4.29\left[\sigma^2 + \beta(0.68t)^3/2\right]^{1/2} \tag{3}$$

The spatial resolution given in Eq. (3) contains 90% of the incident intensity, which is equivalent to full width at tenth maximum (FWTM). The terms σ and β are associated with the incident-beam size and the beam broadening, respectively, and are given by [28]:

$$\sigma = d_{\mathrm{TM}}/4.29, \quad \beta = 500\left(\frac{4\bar{Z}}{E_0}\right)^2\left(\frac{\rho}{\bar{M}}\right) \tag{4}$$

where d_{TM} is the incident beam diameter at FWTM (1.5 nm in the experimental conditions), E_0 is the incident beam energy (in eV), ρ is the specimen density at the measured point, $\bar{Z}$ and $\bar{M}$ are the averaged atomic number and atomic weight, respectively. All of the terms, except for the d_{TM} and E_0 values require the R calculation can be provided by the ζ-factor method. Therefore, the R value can be presented as a map. For the experimental example presented in Fig. 8, the X-ray SI had been obtained from the very thin region (5–15 nm). Thus, the R value is nearly the same as the incident beam size in this case.

In addition to the R calculation, the number of atoms can also be derived from the beam-specimen interaction volume. In the Gaussian beam broadening model, the interaction volume V, which contains 90% of the total electron, can be given as [22, 23, 28, 29]:

$$V = \int_0^t \pi\left[4.29(\sigma^2 + \beta z^3/2)^{1/2}/2\right]^2 dz = \frac{4.29^2\pi}{32}\left(8\sigma^2 t + \beta t^4\right) = 1.81\left(8\sigma^2 t + \beta t^4\right) \tag{5}$$

Since the total number of atoms in the analyzed volume is obtained from $N_{\mathrm{v}}\,\rho V/\bar{M}$ (N_{v}: Avogadro's number), the number of atoms for each element can be determined from the total number of atoms by multiplying the corresponding composition in atomic fraction. It should be noted that the volume determined by Eq. (5) is larger than the cuboid volume at the individual pixels since the X-ray SI was acquired in the oversampling condition, i.e. the beam diameter is larger than the each pixel size in the SI. The maps showing the numbers of total and specific atoms shown in Fig. 8c–f correspond to the cuboid volume at the individual pixels by correcting the difference between the cuboid and the beam-interaction volumes. In this field of view, there are 1000–2200 atoms in total at the individual pixels. However, the minor Ni and Mn constituents comprise less than 200 and 100 atoms, respectively (40–60 Ni atoms and 30–40 Mn atoms in the matrix). For Cu, fewer than 15 atoms and fewer

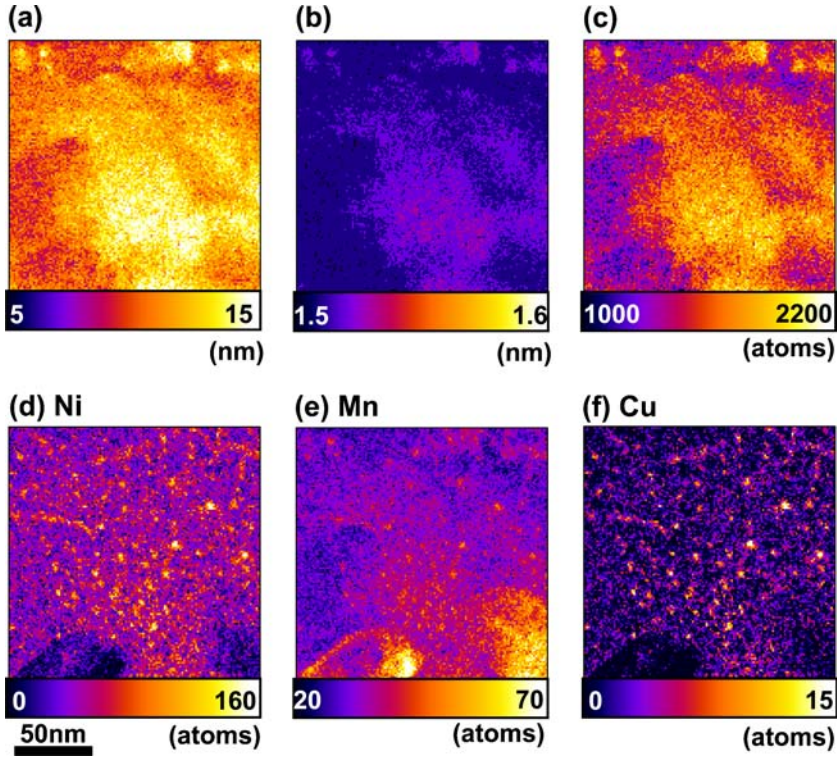

Fig. 8 Advanced maps calculated from the composition maps in Fig. 7: (**a**) thickness map, (**b**) spatial resolution map, (**c**) map of number of total atoms, (**d**) map of number of Ni atoms, (**e**) map of number of Mn atoms and (**f**) map of number of Cu atoms

than 3 atoms can be detected at the precipitate positions and in the matrix, respectively as shown in Fig. 8f. Therefore, the analytical sensitivity in terms of the minimum detectable mass is approaching a few atoms.

Another set of composition maps acquired around a grain boundary (GB) is shown in Fig. 9 (a: Fe, b: Cr, c: Ni, d: Mn, e: Cu and f: Mo). This set of the maps was originally obtained as an X-ray SI. The ζ-factor quantification was applied after the application of the PCA random-noise reduction. There is a fine Cr-rich carbide (~10 nm) in the GB. This carbide also contains Mn and Mo, similarly to the relatively larger carbides in the previously shown maps (Figs. 4, 7, 8). Co-segregation of Ni, Mn, Cu and Mo and corresponding Fe depletion can be seen along the GB in these maps in addition to the presence of the irradiation-induced nanoprecipitates. The major difference in the composition between the irradiation-induced nanoprecipitates and the elemental GB segregation is the presence of Mo, i.e. the irradiation-induced nanoprecipitates do not contain Mo. More interestingly, the irradiation-induced nanoprecipitates are not observed next to the GB, suggesting that there is a type of precipitate-free zone (PFZ) along the GB region due to the GB co-segregation.

The GB segregation can be quantitatively characterized by determining the GB enrichment (GB coverage) Γ^{ex}, which is defined as the number of excess atoms per unit area in the boundary plane. From the compositions of the solute element A and the major element B, the GB enrichment is given as [e.g. 22]:

$$\Gamma_A^{ex} = N_B \frac{C_A}{C_B} \frac{M_B}{M_A} \frac{V}{A} - \Gamma_A^{bk} \quad (6)$$

where Γ^{bk} is the number of solute A atoms per unit area in the bulk, N_B is the number of B atoms per unit volume in the surrounding bulk region, C_A and C_B are the weight fraction for A and B, M_A and M_B are the atomic weights for A and B, and V and A are the interaction volume and the area of the boundary inside the interaction volume, respectively. To determine the V/A term, again the specimen thickness is required. Using the ζ-factor method, the GB enrichment can be extracted from the composition and thickness maps [22]. The extracted GB enrichment maps of selected elements are also shown in Fig. 9 (g: Ni, h: Cu and i: Mo). In these GB enrichment maps, the bulk component Γ^{bk} has been subtracted. The measured GB enrichments of Ni, Mn, Cu and Mo are 8.00 ± 1.00, 1.36 ± 0.13, 0.69 ± 0.06 and 0.18 ± 0.03 atoms/nm^2, which correspond to 0.42 ± 0.05, 0.072 ± 0.007, 0.036 ± 0.003 and 0.009 ± 0.002 monolayers, respectively. Note that a single monolayer contains ~19 atoms/nm^2 in this steel.

The nanoprecipitate composition estimated from Figs. 7 and 9 is: ~30 wt% Ni–4-to-5% Mn–4-to-5% Cu (bal Fe) whereas the mean composition measured via 3D-APFIM was approximately 28% Ni–10% Mn–4% Cu–3% Si–55%

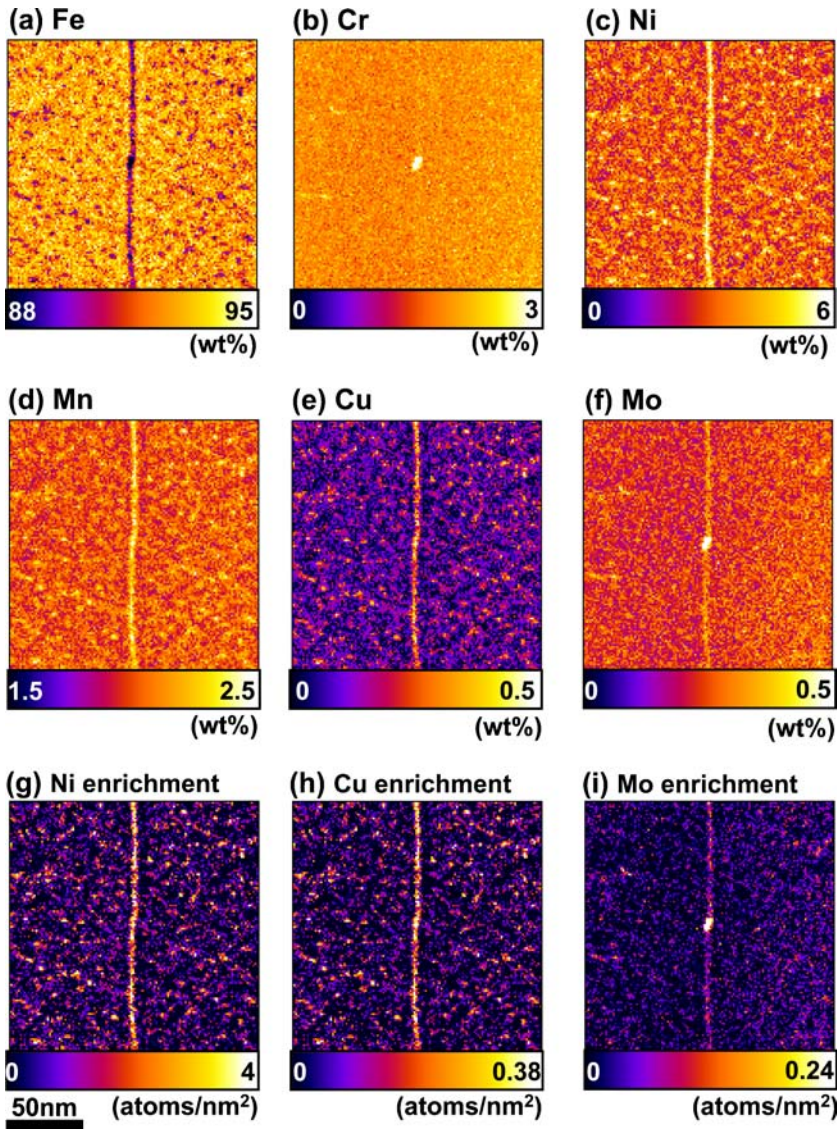

Fig. 9 A series of composition maps and advanced maps obtained around a GB in the irradiated low-alloy steel. These maps were originally acquired as an X-ray SI and quantified by the ζ-factor method after the PCA random-noise reduction was performed. Composition maps of (**a**) Fe, (**b**) Cr, (**c**) Ni, (**d**) Mn, (**e**) Cu, (**f**) Mo, and the GB enrichment maps of (**g**) Ni, (**h**) Cu and (**i**) Mo

Fe. The compositions determined from the X-ray maps are close to those measured via 3D-APFIM, except for Mn. The discrepancy in the Mn content is due to the artificial increase in the matrix Mn X-ray signal from the radioactive Fe^{55} (created by the neutron irradiation), which generates Mn Kα X-rays. The 3D-APFIM technique is capable of both single-atom detection and atomic-scale spatial resolution simultaneously. On the other hand, in conventional STEM-EDX mapping, neither single-atom detection nor atomic resolution analysis has yet been achieved. However, the results presented in Figs. 7 and 8 are nearly comparable with those from the 3D-APFIM. In addition, there is a significant advantage to the FEG-STEM EDX technique in that the sampling area size is larger so that more nano-scale features can be analyzed in any one acquisition.

Conclusions

The use of MSA and ζ-factor methods successfully permitted the quantification of X-ray maps to reveal the presence of nanoprecipitates in the irradiated A508 G4N steel. These quantified X-ray maps obtained from the HB603 FEG-STEM enabled the measurement of the nanoprecipitate sizes, and an assessment of the number density of nanoprecipitates. The size of the irradiation-induced nanoprecipitates detected ranged from ~2 nm to ~4 nm. The use of the ζ-factor method enabled the thickness of the sample to be determined as a function of location, so that the number density of nanoprecipitates could be measured. The number density of nanoprecipitates was approximately 2×10^{23} m^{-3}. These results are in

remarkably good agreement with the sizes and number density as measured via 3D-AP.

The most significant aspect of the MSA/PCA-processed quantified X-ray maps was the ability to clearly discern the presence of Cu and Mn in the nanoprecipitates, thereby providing an independent confirmation of the atom probe data. This is the first time that the FEG-STEM EDX technique has been successfully used to detect and quantify these irradiation-induced nanoprecipitates. Furthermore, the quantified X-ray maps also showed that existing dislocations in this complex, tempered lath structure could serve as preferential sites for the formation of nanoprecipitates. This highlights another major advantage of the FEG-STEM EDX technique over the 3D-APFIM: vastly improved sampling (larger areas of analysis).

It is clear that the improvements in spectral quantification afforded by the ζ-factor method coupled with the MSA/PCA technique—in addition to the on-going developments in Cs-correction for finer probes—will provide new opportunities for moving FEG-STEM EDX characterization into the realm of what was previously considered the exclusive domain of atom probe field-ion microscopy.

Acknowledgements The authors wish to acknowledge the support of the National Science Foundation through grants (DMR-0320906 and DMR-0304738) and Bechtel Bettis, Inc.

References

1. Burke MG, Brenner SS (1986) J Physique 34(C2):239
2. Burke MG, Stofanak RJ, Hyde JM, English CA, Server WL (2001) In: Was GS (ed) Proc. 10th Intl. Symposium on Environmental Degradation of Materials in Nuclear Power Systems—Water Reactors, NACE, CD
3. Blavette D, Deconihout B, Bostel A, Sarrau JM, Bouet M, Menand A (1993) Rev Sci Instrum 64:2911
4. Cerezo A, Godfrey TJ, Smith GDW (1988) Rev Sci Instrum 59:862
5. Miller MK, Cerezo A, Hetherington MG, Smith GDW (1996) Atom probe field-ion microscopy. Oxford University Press, New York
6. Miller MK (2000) Atom probe tomography. Kluwer Academic Publishers, New York
7. Kelly TF, Gribb TT, Olson JD, Martens RL, Shepard JD, Wiener SA, Kunicki TC, Ulfig RM, Lenz DR, Strennen EM, Olman E, Bunton JH, Strait DR (2004) Microsc Microanal 10:373
8. Miller MK (2005) Microsc Microanal 11(Suppl. 2):628
9. Miller MK, Burke MG (1992) J Nucl Matter 195:68
10. Pareige P, Auger P, Miloudi S, van Duysen JC, Akamatsu M (1997) Ann Phys C2–22(117–124):8
11. Hyde JM, English CA, (2001) Mater Res Soc Symp Proc 650:R6.61
12. Jeanguillaume C, Colliex C (1989) Ultramicroscopy 28:252
13. Hunt JA, Williams DB, (1991) Ultramicroscopy 38:47
14. Jolliffe IT (2002) Principal component analysis. 2nd edn. Springer, New York
15. Malinowski ER (2002) Factor analysis in chemistry. 3rd edn. Wiley, New York
16. Trebbia P, Bonnet N (1990) Ultramicroscopy 34:165
17. Titchmarsh JM, Dumbill S (1996) J Microsc 184:195
18. Titchmarsh JM (1999) Ultramicroscopy 78:241
19. Kotula PG, Keenan MR, Michael JR (2003) Microsc Microanal 9:1
20. Fiori CE, Swyt CR, Myklebust RL (1992) NIST/NIH Desk top spectrum analyzer, available from the National Institute of Standards and Technology Gaithersburg, MD 20899, USA, (1992). (http://www.micro.nist.gov/DTSA/dtsa.html)
21. Watanabe M, Williams DB (1999) Microsc Microanal 5(Suppl. 2):88
22. Watanabe M, Williams DB (2003) Z Metallk 94:307
23. Watanabe M, Williams DB (2006) J Microsc 221:89
24. Reed WP (1993) Certificate of analysis for standard reference material 2063a. National Institute of Standards and Technology, Gaithersburg, MD 20899, USA
25. Cochran RN, Horne FH (1977) Anal Chem 49:846
26. Keenan MR, Kotula PG (2004) Surf Interface Anal 36:203
27. Keast VJ, Williams DB (2000) J Microsc 199:45
28. Doig P, Flewitt PEJ (1982) Metal Trans A 13:1397
29. van Cappellan E, Schmitz A (1992) Ultramicroscopy 41:193